PHOTONICS Research

Silicon nonlinear switch as a conditional circulator for monostatic LiDAR systems

Mingfei Ding,[1] Yiwei Xie,[1,2,*] Hao Yan,[1] Abu Naim R. Ahmed,[3] Reza Safian,[3] Swapnajit Chakravarty,[3] Leimeng Zhuang,[3] Pengcheng Jiao,[4] Huan Li,[1] Liu Liu,[1] and Daoxin Dai[1,2]

[1]Centre for Optical and Electromagnetic Research, State Key Laboratory for Modern Optical Instrumentation, Zhejiang Provincial Key Laboratory for Sensing Technologies, Zhejiang University, Zijingang Campus, Hangzhou 310058, China
[2]Ningbo Research Institute, Zhejiang University, Ningbo 315100, China
[3]imec USA, Nanoelectronics Design Center, Inc., Kissimmee, Florida 34744, USA
[4]Ocean College, Zhejiang University, Zhoushan 316021, China
*Corresponding author: xieyiw@zju.edu.cn

Received 29 September 2021; revised 20 November 2021; accepted 13 December 2021; posted 13 December 2021 (Doc. ID 444480); published 24 January 2022

All-optical silicon-photonics-based LiDAR systems allow for desirable features in scanning resolution and speed, as well as leverage other advantages such as size, weight, and cost. Implementing optical circulators in silicon photonics enables bidirectional use of the light path for both transmitters and receivers, which simplifies the system configuration and thereby promises low system cost. In this work, to the best of our knowledge, we present the first experimental verification of all-passive silicon photonics conditional circulators for monostatic LiDAR systems using a nonlinear switch. The proposed silicon nonlinear interferometer is realized by controlling signal power distribution with power-splitting circuits, allowing the LiDAR transmitter and receiver to share the same optical path. Unlike the traditional concept requiring a permanent magnet, the present device is implemented by using common silicon photonic waveguides and a standard foundry-compatible fabrication process. With several additional phase shifters, the demonstrated device exhibits considerable flexibility using a single chip, which can be more attractive for integration with photodetector arrays in LiDAR systems. © 2022 Chinese Laser Press

https://doi.org/10.1364/PRJ.444480

1. INTRODUCTION

Light detection and ranging (LiDAR) is considered as a revolutionary technology for automated systems interacting with their environments and users, due to the directivity and focusing of the beam during its propagation [1,2]. To date, most of the reported LiDAR systems are typically large and expensive. A chip-scale LiDAR system that fits on a fingertip footprint and is exponentially scalable to affordable volume production has been the primary pursuit recently. In addition to improving reliability and having lower cost, LiDAR on a chip also potentially features a higher range, lower noise, and better resolution than today's bulky LiDAR systems [3].

In an on-chip LiDAR system, optical circulators are one of the key elements providing the control and management of signal functionalities, i.e., routing the transmitted light beam toward the aperture and the reflected light beam from the aperture to photodetectors [4]. Great efforts have been made to develop circulator devices in photonic integrated circuits (PICs) with, e.g., magneto-optic effects [5–8], spatiotemporal modulation [9–13], optical nonlinearities [14–16], and opto-mechanical implementations including typical resonator architectures [17–19]. However, it remains a great challenge to realize low-loss, efficient, and compact photonic circulators in PICs. Magneto-optic approaches, which require an external magnetic field and a magnetic-field shield, are intrinsically lossy and not fully compatible with complementary metal–oxide–semiconductor (CMOS) technology [20,21]. Approaches based on spatiotemporal modulation have been proved promising for complete on-chip nonreciprocity, but they suffer from significant power consumption and complicated electro-optical driving systems [22]. Other approaches such as all-passive metasurfaces and chiral interactions have also been demonstrated [23,24], but the complexity of the design and integration with the PIC platform are challenging. Recently, silicon photonics has been seen as a key platform for complex PICs because of its CMOS compatibility as well as ultra-dense on-chip integration [25]. Also, with high optical Kerr nonlinearities, silicon photonics has been extensively explored in all-optical signal processing and switching [26]. Benefitting from the high nonlinear response of silicon nanophotonic waveguides, power-dependent nonlinear effects such as Brillouin-induced transparency [27], optomechanical-induced transparency [28,29], or the nonlinear Kerr effect in resonant

structures [30–32] have been introduced to act as non-reciprocal functionality on silicon. So far, these circulator realization approaches have been mostly demonstrated in non-reciprocal devices such as isolators. Yet, very few implementations have been carried out on circulators in PICs, especially in the silicon photonic platform, which are promising to meet the needs for future large-scale photonic integration, particularly for emerging LiDAR-driven applications.

In this paper, we report novel silicon photonic nonlinear switches as conditional circulators for monostatic LiDAR systems by using a Mach–Zehnder interferometer (MZI) with the Kerr effect. The basic principle is to utilize the interference of two signals with different nonlinearity-induced phase changes on two arms of the nonlinear MZI (NMZI) switch by controlling the signal power with power-splitting circuits. This design is foundry compatible with regular passive silicon waveguide components only and has better wavelength independence than our previous design based on subwavelength grating (SWG) waveguides [33]. Compared with previously demonstrated approaches, the present conditional circulator based on nonlinear optical effects is expected generically for the chip system with broken Lorentz reciprocity [34,35]. This silicon-based conditional circulator featuring intensity-dependent $\chi^{(3)}$ nonlinearity enables counter-propagated signal routing for LiDAR systems, allowing low excess loss and a high SNR that is critical to transceiver module performance.

In particular, different from traditional bistatic LiDAR systems with one transmitter and one receiver side by side, it is often desired to develop one with a single-aperture lens used for both transmitting and receiving for saving weight and space, called a monostatic LiDAR system [36]. While various commercial circulators utilizing dual/multiple aperture transceivers provide a potential solution [37,38], they have not shown an acceptable trade-off in characteristics requiring high-power handling and a wide field of view, as well as eliminating blind spots. In our architectures, the transmitted high-power pulse counters with the received low-power pulse with the same aperture lens, but they have different phase delays due to different optical nonlinearities. This device enables a single-aperture transceiver with closely spaced waveguides placed near the focal point of a single objective to form input and detector apertures. This compact characteristic enables the device more power efficiency, more position accuracy, and more accessibility to achieve full on-chip integration. Moreover, phase-shifter-based tuning elements are added to increase the reconfigurability of the switch for selecting the desirable output [39]. It is expected that the present conditional circulator based on a nonlinear silicon switch with the Kerr effect will play a very important role in chip-based time-of-flight (ToF) LiDAR as well as reconfigurable optical networks with large-scale photonic-switch arrays.

2. PRINCIPLE AND STRUCTURE

A. Principle

Figure 1 demonstrates the principle of the designed NMZI switch. The device is made up of three sections as depicted in Fig. 1(a), i.e., a tunable 2 × 2 coupler based on MZIs, two arms with different nonlinear effects, and another tunable 2 × 2 coupler. It contains four ports used for input and output

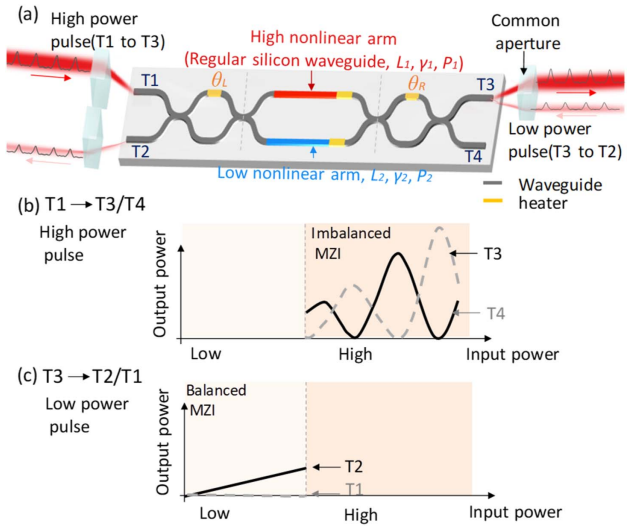

Fig. 1. (a) Schematic of NMZI switch with two arms of different nonlinear effects; relationship between input power from T1 and output power from T3/T4 when the input is (b) high-power and (c) low-power pulses.

coupling. A normal silicon strip waveguide with a high nonlinear Kerr coefficient is used for one of the MZI arms, while the other arm is based on the waveguide structure with a reduced nonlinear effect. As shown in Figs. 1(b) and 1(c), for a low-power input pulse, the NMZI switch is balanced (two arms have the same phase), and the output power of the cross port is proportional to the input signal. When the input power gradually increases, the self-phase modulation (SPM) nonlinear effect becomes enhanced, and the NMZI switch turns into an imbalanced state, resulting from the power-dependent phase change in the MZI's arm. In other words, the output power of the NMZI switch oscillates between the maxima and minima as the input power increases.

The transfer function of the device is given by

$$H = H_L \begin{bmatrix} \alpha L_1 \cdot \exp(-i\varphi_1) & 0 \\ 0 & \alpha L_2 \cdot \exp(-i\varphi_2) \end{bmatrix} H_R, \quad (1)$$

where $H_{L,R}$ is the transfer function of the left and right sides of the 2 × 2 couplers in the NMZI switch, which can be described as

$$H_{L,R} = \begin{bmatrix} \sqrt{0.5} & -j\sqrt{0.5} \\ -\sqrt{0.5} & \sqrt{0.5} \end{bmatrix} \begin{bmatrix} e^{-j\theta_{L,R}} & 0 \\ 0 & 1 \end{bmatrix} \begin{bmatrix} \sqrt{0.5} & -j\sqrt{0.5} \\ -\sqrt{0.5} & \sqrt{0.5} \end{bmatrix}$$
$$= 0.5 \begin{bmatrix} -1 + e^{-j\theta_{L,R}} & -j(1 + e^{-j\theta_{L,R}}) \\ -j(-1 + e^{-j\theta_{L,R}}) & -1 + e^{-j\theta_{L,R}} \end{bmatrix}, \quad (2)$$

where $\theta_{L,R}$ is the phase difference in the arm of left and right sides of the 2 × 2 couplers, $\varphi_{1,2}$ are the nonlinear phase changes on the MZI's arm based on the SPM nonlinear effect, and subscripts 1 and 2 are upper and lower arm of the NMZI switch, respectively. The nonlinear phase change, φ, is given as [40]

$$\varphi = \gamma P L_{\text{eff}}, \quad (3)$$

where P is the peak power of the input signal, γ is the nonlinear coefficient, and L_{eff} is the effective length of the arm in the NMZI. At the output, interference between the signals with different phase delays happens, and thus the output power is strongly dependent on the input power. L_{eff} is the effective length depending on the propagation loss α and the arm length L, and one has $L_{\text{eff}} = [1 - \exp(-\alpha L)]/\alpha$. The nonlinear coefficient γ is given by [41–43]

$$\gamma = \frac{2\pi \bar{n}_2}{\lambda A_{\text{eff}}}, \tag{4}$$

where the effective mode area A_{eff} is given by

$$A_{\text{eff}} = \frac{|\int[(e_v \times h_v^*) \cdot \hat{z}\mathrm{d}A]|^2}{\int |(e_v \times h_v^*) \cdot \hat{z}|^2 \mathrm{d}A}, \tag{5}$$

where e_v and h_v are field distributions. The nonlinear refractive index $\bar{n}_2$ is averaged over an inhomogeneous cross section weighted with respect to the field distribution as

$$\bar{n}_2 = k\left(\frac{\varepsilon_0}{\mu_0}\right) \frac{\int n^2(x,y) n_2(x,y)(2|e_v|^4 + |e_v^2|^2)\mathrm{d}A}{3\int |(e_v \times h_v^*) \cdot \hat{z}|^2 \mathrm{d}A}, \tag{6}$$

where k is the wave number, ε_0 is the permittivity of vacuum, and μ_0 is the permeability of vacuum.

When the transmitted high-power and received low-power pulses counter-propagate through the NMZI switch from T1 and T3 ports, respectively, the high-power signal experiences a Kerr-effect-induced phase change; if the phase difference between two arms becomes π, it will be output from T3 port, while the low-power signal experiences no phase change and is output from NMZI cross port T2. In this case, by properly choosing signal powers, the NMZI switch operates passively to allow the LiDAR transmitter/receiver to share the same lens aperture, which greatly reduces the complexity and cost of the system. This compact characteristic enables the device more power efficiency and more position accuracy. If a high-power pulsed-cycle signal and low-power pulsed-cycle signal have overlap in the time domain, both the high-power signal and low-power signal experience phase change due to the Kerr effect related to power intensity. In this case, the high-power forward pulse dominates the phase change accumulation for both pulses. This happens only for the duration of overlap, and it is likely to happen in the one-path arm, as the eight-sub-path has very low power for both forward and reflected pulses. This may eventually affect the extinction ratio of the switch or cause additional overall loss, and it is a concern for the system design and should be included in power budget and SNR considerations. In practice, the phase shifters on two 2×2 couplers can be tuned to compensate for this effect (i.e., change the extinction ratio of the NMZI switch), so that the received low-power pulses can be detected. Thus, high SNR can be achieved without worrying about the level of isolation between the transmitter and receiver. Also, this architecture improves the detector response to the return signal because of the effective overlap between the receiver and transmitter. Moreover, phase shifters are added on MZI arms to minimize the random phase on the arms, and shift the output power response versus input power. This characteristic enables arbitrary power of a high-power pulse to be selected as the transmitted signal input from port T1 using the proposed switch. This re-configurability is indispensable for complete integration when the complexity and versatility of LiDAR systems increase.

B. Structure

The principle for designing the NMZI switch is to achieve different phase changes induced by nonlinear photonic effects in two arms. The nonlinear phase change depends on the input power, nonlinear coefficient, and effect length of the waveguide, as indicated by Eq. (3). In Ref. [33], we implemented a nonlinear switch by controlling the nonlinear coefficient with an SWG waveguide. However, SWG introduces additional losses and suffers fabrication imperfection, which results in a low-extinction-ratio NMZI switch. In this paper, we propose a novel design using power splitters, as shown in Fig. 2. In this design, eight waveguide branches are introduced on one of the NMZI arms so that the power P on each branch is reduced; thus, the phase accumulations on NMZI's two arms are different, regarding that the Kerr-effect-induced phase change strongly depends on the power density. Accordingly, separate thermal tuning units (phase shifters) are utilized to synchronize the signals by compensating for phase errors due to fabrication imperfection before recombining. In this case, additional power consumption is introduced. Fortunately, the power consumption can be reduced dramatically by using a low-phase-error waveguide design, as demonstrated previously [44]. Finally, one achieves input-power-dependent outputs at the two ports. The two arms of the NMZI are still balanced when there is no nonlinear-effect-induced phase change (i.e., low-power input power). Considering the chip size and performability of the device, we fix one 2×2 coupler as a 3 dB coupler, and the other 2×2 coupler is tunable.

Figures 3(a) and 3(b) show the chip layout and the microscope photo of the NMZI switch. This proof-of-concept chip was fabricated on a silicon-on-insulator (SOI) platform using the processing flow provided by a commercial fabrication service (ANT NanoSOI [45]). The SOI wafer used here has a 220 nm thick top-silicon layer and a 2 μm thick SiO_2 buried-oxide (BOX) layer. The waveguide cross section size is 220 nm × 500 nm (height × width) to support the fundamental TE mode, and an NMZI switch arm length is selected as 15.6 mm in terms of balancing the nonlinear effects with loss and size. The effective area A_{eff} of the fundamental mode is calculated to be 0.065 μm^2. Using the nonlinear index in a silicon waveguide of $n_2 = 4.5 \times 10^{-18}\ m^2\,W^{-1}$, the nonlinear coefficient is calculated to be 282 $m^{-1}\,W^{-1}$ at 1550 nm. The waveguide loss is measured as 2.7 dB/cm. The input/output ports have edge couplers for efficient chip–fiber coupling, and the coupling loss is around 8 dB including both couple-in and

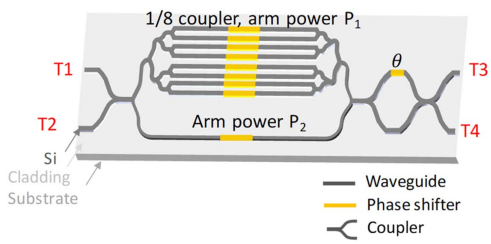

Fig. 2. NMZI switch with 1/8 coupler on one arm.

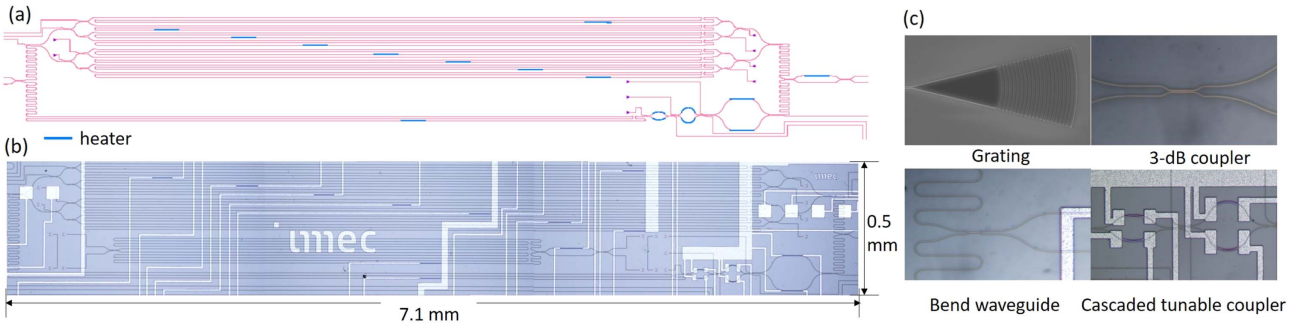

Fig. 3. Picture of (a) chip layout and (b) fabricated chip of NMZI switch; (c) component structures of the NMZI switch.

Table 1. Parameters in the NMZI Switch

Parameter	Value
Waveguide loss α (dB/cm)	2.7
Fiber-to-chip coupling loss (dB)	8
Effective area A_{eff} (μm^2)	0.065
Arm length L (mm)	15.6
Nonlinear refractive index of Si n_2 (m^2/W)	4.5×10^{-18}
Effective nonlinear coefficient γ of strip silicon photonic waveguide (W^{-1} m^{-1})	282

-out losses. For easy device characterization purposes, we add some testing ports to monitor the power on the circuit, as can be seen in Fig. 3(a). To realize a more efficient tuning process in the future, simplified and robust architectures and automatic algorithms are very desired. For example, it is possible to introduce low-phase-error tuning elements [44], which possibly enables calibration-free basic building blocks. The metal pads of 100 μm × 100 μm are placed with a pitch of 200 μm. In addition, we used the fabricator's process design kit (PDK) verified 3 dB directional couplers to split and combine the signal. The balance among the chip area, possible inter-component cross talk, and efficient routing of both optical and electrical paths is optimized. In particular, an S-shaped spiral with a bend radius of 9 μm is used for the MZI's arm to minimize the waveguide bend loss and the area simultaneously, as shown in Fig. 3(c). In the lower arm of the MZI, a cascade of three tunable directional couplers is employed. These couplers use the same bends as in the upper MZI arm to make sure of equal path lengths between the two arms. In addition, the tuning requirement of this circuit section can be split over the three couplers, which reduces the risk of tuning failure. Table 1 gives the parameters for the present design.

3. EXPERIMENTAL RESULTS

Figure 4 shows the experimental setup for device characterization and function verification of the NMZI switch. First, the device operation bandwidth verification is performed. A CW light from a tunable laser passes through a polarizer and then is coupled into the chip through an input edge coupler via port T1. The power of the CW laser is fixed at 15 dBm. The output power from ports T3 and T4 of the switch was measured by a power meter. We varied the wavelength from 1545 nm to 1560 nm, over a bandwidth of 15 nm. The phase shifters on the arms of the 2 × 2 coupler are tuned to achieve the maximum T4-to-T3 extinction ratio of the NMZI switch. The theoretical [using Eq. (1)] and measured results are given in Fig. 5, where the measured output powers of T3 and T4 ports are quite uniform around 5 dBm and −13 dBm, respectively, showing a good agreement with theory over the bandwidth of interest. In this case, the NMZI switch is in a balanced state, and most of the signal is output from cross port T4.

Then, a pulsed laser with pulse width, rate, power, etc., is used to verify the nonlinear switch function. The pulsed laser (Lumentum ERGO) at 10 Gpulses/s with a pulse duration of 2 ps is used as a pulse source input into the NMZI chip. The total power of the pulsed laser ranges from 60 mW to 160 mW. Figure 6(a) shows the measured transmissions at the output ports (T3 and T4) of the NMZI switch with respect to input power. As explained in Eq. (3), the higher the input power, the greater the phase difference between the lower MZI arm (single path) and upper MZI arm (sub-splitting), owing to

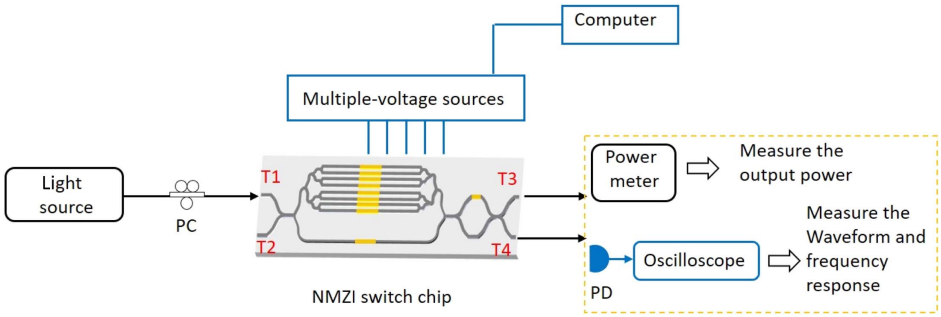

Fig. 4. Experimental setup for optical NMZI switch. PC, polarization controller; CW, continuous waveform.

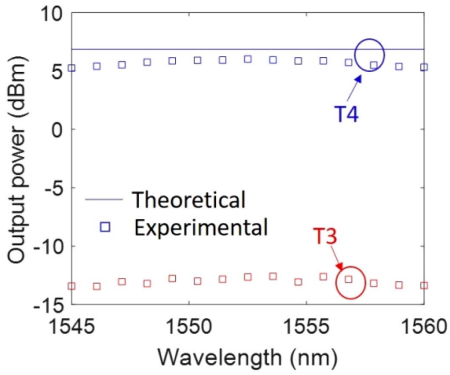

Fig. 5. Output power at port T3/T4 of NMZI switch with respect to input signal wavelength (low-power signal input) for different wavelengths.

the power-dependent SPM nonlinear effect. As shown in Fig. 6(a), the entire NMZI works as a power-dependent switch, and the output power difference maxima happen when the two MZI arms have in-phase or out-of-phase status. Figure 6(b) shows the T3-to-T4 power extinction ratio in dB, with a maximum of 20 dB within 15 nm wavelength ranging, verifying the switch function with good performance. Some other options based on bend directional couplers (DCs) or broadened multi-mode interferometer (MMI) couplers demonstrated recently [44,46] can be used to have improved fabrication tolerance. Furthermore, using the phase shifters across all NMZI's arms, one can adjust the initial inter-arm phase difference such that the extinction versus input power relation shifts properly to make sure maximum extinction occurs at the target port for a given input power, as shown in the dashed lines in Fig. 6.

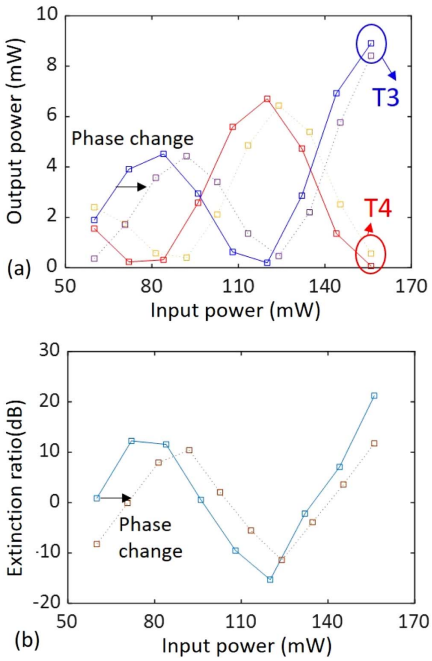

Fig. 6. Experimental results of the NMZI switch with the input of a pulsed light source: (a) output powers versus input powers at T3 and T4; (b) T3-to-T4 extinction ratio in dB.

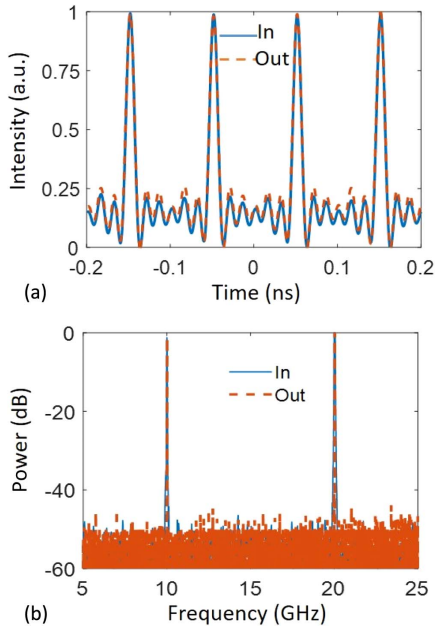

Fig. 7. Measured waveform and signal spectra obtained from a photodetector: (a) waveform before the chip and chip output port T3; (b) spectra before the chip and chip output port T3.

Furthermore, a signal fidelity experiment was performed. The experimental setup is shown in Fig. 4. The pulsed laser with a repetition rate of 10 Gpulses/s is used as the input. Figures 7(a) and 7(b) show the measured waveform and spectra, respectively, of the pulses at the input and output ports of the NMZI switch. The corresponding signal spectrum and waveform obtained by means of a 40 GHz photodetector (xpdv2120ra) were measured using a 160 GSa/s, 50 GHz real-time oscilloscope (Agilent DSO-X 95004Q). It can be seen that the NMZI switch introduces negligible signal degradation, which verifies the feasibility of the proposed device for practical use.

Here, the SPM-induced spectral broadening should be considered for the case with very high input power, which results in power consumption of the overall system. Apart from power dependence, the lifetime of the generated carriers here is another critical parameter that affects the SPM process. For data rates higher than 1 Gb/s, SPM-induced spectral broadening might decrease [47]. To reduce the SPM-induced spectral broadening further, the potential solution is to use a low-repetition-rate pulse source with high peak power, so that better performance can be expected because the total nonlinear absorption losses become fewer. Moreover, by properly designing the waveguide width and number of branches, the NMZI switch will have more tolerance towards the power of input signals.

4. CONCLUSION

In this paper, an NMZI switch is proposed and verified experimentally, with investigation of its function when using both CW laser and pulsed light sources. It is shown that the power at the output ports of an NMZI switch varies between maxima

and minima with the increase in input power. Using the phase shifters in the device, the NMZI switch can be adjusted to work with different input powers and provide a switch extinction ratio of 20 dB, which are interesting features pointing to practical use. This work builds up signal processing functions in silicon photonics technology and contributes useful components for future on-chip LiDAR systems.

Funding. National Key Research and Development Program of China (2019YFB2203604); National Science Fund for Distinguished Young Scholars (61725503); Zhejiang Provincial Natural Science Foundation (LZ18F050001); National Natural Science Foundation of China (91950205, 6191101294, 11861121002, 61905209, 62175214); International Cooperation and Exchange Programme NSFC-RS (62111530147).

Acknowledgment. We thank imec USA for conceiving the device concept and providing the layout design.

Disclosures. The authors declare no conflicts of interest.

Data Availability. Data underlying the results presented in this paper are not publicly available at this time but may be obtained from the authors upon reasonable request.

REFERENCES

1. "LiDAR drives forwards," Nat. Photonics **12**, 441 (2018).
2. A. Martin, D. Dodane, L. Leviandier, D. Dolfi, A. Naughton, P. O'Brien, T. Spuessens, R. Baets, G. Lepage, P. Verheyen, P. D. Heyn, P. Absil, P. Feneyrou, and J. Bourderionnet, "Photonic integrated circuit-based FMCW coherent LiDAR," J. Lightwave Technol. **36**, 4640–4645 (2018).
3. C. V. Poulton, A. Yaacobi, D. B. Cole, M. J. Byrd, M. Raval, D. Vermeulen, and M. R. Watts, "Coherent solid-state LIDAR with silicon photonic optical phased arrays," Opt. Lett. **42**, 4091–4094 (2017).
4. P. Pintus, D. Huang, C. Zhang, Y. Shoji, T. Mizumoto, and J. E. Bowers, "Microring-based optical isolator and circulator with integrated electromagnet for silicon photonics," J. Lightwave Technol. **35**, 1429–1437 (2017).
5. L. Bi, J. Hu, P. Jiang, D. H. Kim, G. F. Dionne, L. C. Kimerling, and C. A. Ross, "On-chip optical isolation in monolithically integrated non-reciprocal optical resonators," Nat. Photonics **5**, 758–762 (2011).
6. Y. Shoji and T. Mizumoto, "Magneto-optical non-reciprocal devices in silicon photonics," Sci. Technol. Adv. Mater. **15**, 014602 (2014).
7. Z. Wang and S. Fan, "Optical circulators in two-dimensional magneto-optical photonic crystals," Opt. Lett. **30**, 1989–1991 (2005).
8. J. Y. Chin, T. Steinle, T. Wehlus, D. Dregely, T. Weiss, V. I. Belotelov, B. Stritzker, and H. Giessen, "Non-reciprocal plasmonics enables giant enhancement of thin-film Faraday rotation," Nat. Commun. **4**, 1599 (2013).
9. Z. Yu and S. Fan, "Complete optical isolation created by indirect interband photonic transitions," Nat. Photonics **3**, 91–94 (2009).
10. H. Lira, Z. Yu, S. Fan, and M. Lipson, "Electrically driven nonreciprocity induced by interband photonic transition on a silicon chip," Phys. Rev. Lett. **109**, 033901 (2012).
11. D. L. Sounas and A. Alù, "Non-reciprocal photonics based on time modulation," Nat. Photonics **11**, 774–783 (2017).
12. A. Mock, D. Sounas, and A. Alù, "Magnet-free circulator based on spatiotemporal modulation of photonic crystal defect cavities," ACS Photon. **6**, 2056–2066 (2019).
13. I. A. D. Williamson, M. Minkov, A. Dutt, J. Wang, A. Y. Song, and S. Fan, "Integrated non-reciprocal photonic devices with dynamic modulation," Proc. IEEE **108**, 1759–1784 (2020).
14. E. A. Kittlaus, N. T. Otterstrom, P. Kharel, S. Gertler, and P. T. Rakich, "Non-reciprocal interband Brillouin modulation," Nat. Photonics **12**, 613–619 (2018).
15. E. A. Kittlaus, P. O. Weigel, and W. M. Jones, "Low-loss nonlinear optical isolators in silicon," Nat. Photonics **14**, 338–339 (2020).
16. P. Aleahmad, M. Khajavikhan, D. Christodoulides, and P. LiKamWa, "Integrated multi-port circulators for unidirectional optical information transport," Sci. Rep. **7**, 2129 (2017).
17. F. Ruesink, J. P. Mathew, M.-A. Miri, A. Alù, and E. Verhagen, "Optical circulation in a multimode optomechanical resonator," Nat. Commun. **9**, 1798 (2018).
18. Z. Shen, Y.-L. Zhang, Y. Chen, F.-W. Sun, X.-B. Zou, G.-C. Guo, C.-L. Zou, and C.-H. Dong, "Reconfigurable optomechanical circulator and directional amplifier," Nat. Commun. **9**, 1797 (2018).
19. M. Hafezi and P. Rabl, "Optomechanically induced non-reciprocity in microring resonators," Opt. Express **20**, 7672–7684 (2012).
20. S. Ghosh, S. Keyvavinia, W. Van Roy, T. Mizumoto, G. Roelkens, and R. Baets, "Ce:YIG/silicon-on-insulator waveguide optical isolator realized by adhesive bonding," Opt. Express **20**, 1839–1848 (2012).
21. T. Mizumoto, R. Baets, and J. E. Bowers, "Optical non-reciprocal devices for silicon photonics using wafer-bonded magneto-optical garnet materials," MRS Bull. **43**, 419–424 (2018).
22. E. Verhagen and A. Alù, "Optomechanical nonreciprocity," Nat. Phys. **13**, 922–924 (2017).
23. M. Scheucher, A. Hilico, E. Will, J. Volz, and A. Rauschenbeutel, "Quantum optical circulator controlled by a single chirally coupled atom," Science **354**, 1577–1580 (2016).
24. D. L. Sounas, C. Caloz, and A. Alù, "Giant non-reciprocity at the subwavelength scale using angular momentum-biased metamaterials," Nat. Commun. **4**, 2407 (2013).
25. W. Bogaerts and L. Chrostowski, "Silicon photonics circuit design: methods, tools and challenges," Laser Photon. Rev. **12**, 1700237 (2018).
26. J. Leuthold, C. Koos, and W. Freude, "Nonlinear silicon photonics," Nat. Photonics **4**, 535–544 (2010).
27. C.-H. Dong, Z. Shen, C.-L. Zou, Y.-L. Zhang, W. Fu, and G.-C. Guo, "Brillouin-scattering-induced transparency and non-reciprocal light storage," Nat. Commun. **6**, 6193 (2015).
28. F. Ruesink, M.-A. Miri, A. Alù, and E. Verhagen, "Nonreciprocity and magnetic-free isolation based on optomechanical interactions," Nat. Commun. **7**, 13662 (2016).
29. E. A. Kittlaus, W. M. Jones, P. T. Rakich, N. T. Otterstrom, R. E. Muller, and M. Rais-Zadeh, "Electrically driven acousto-optics and broadband non-reciprocity in silicon photonics," Nat. Photonics **15**, 43–52 (2021).
30. A. Li and W. Bogaerts, "Reconfigurable nonlinear non-reciprocal transmission in a silicon photonic integrated circuit," Optica **7**, 7–14 (2020).
31. K. Xia, F. Nori, and M. Xiao, "Non-reciprocal propagation of light in a chiral optical cross-Kerr nonlinear medium," in *14th Pacific Rim Conference on Lasers and Electro-Optics (CLEO PR)* (Optical Society of America, 2020), paper C12C_13.
32. K. Y. Yang, J. Skarda, M. Cotrufo, A. Dutt, G. H. Ahn, M. Sawaby, D. Vercruysse, A. Arbabian, S. Fan, A. Alù, and J. Vučković, "Inverse-designed non-reciprocal pulse router for chip-based LiDAR," Nat. Photonics **14**, 369–374 (2020).
33. M. Ding, Y. Xie, C. Zhang, M. Teng, A. N. R. Ahmed, R. Safian, S. Chakravarty, P. Jiao, D. Dai, and L. Zhuang, "Silicon photonics nonlinear switch as conditional circulator for single-aperture LIDAR systems," Proc. SPIE **11691**, 116910L (2021).
34. Y. Shi, Z. Yu, and S. Fan, "Limitations of nonlinear optical isolators due to dynamic reciprocity," Nat. Photonics **9**, 388–392 (2015).
35. A. Srivastava, P. P. Paltani, and S. Medhekar, "Switching behaviour of a nonlinear Mach-Zehnder interferometer," Pramana **74**, 575–590 (2010).
36. H. Ahmed, S. Balbina, and Y. H. Yasser, "Monostatic and bistatic lidar systems: simulation to improve SNR and attainable range in daytime operations," Proc. SPIE **10094**, 1009421 (2017).
37. C. F. Abari, X. Chu, R. Michael Hardesty, and J. Mann, "A reconfigurable all-fiber polarization-diversity coherent Doppler lidar: principles and numerical simulations," Appl. Opt. **54**, 8999–9009 (2015).

38. J. M. Roth, R. E. Bland, and S. I. Libby, "Large-aperture wide field of view optical circulators," IEEE Photon. Technol. Lett. **17**, 2128–2130 (2005).
39. Y. Zhao, X. Wang, D. Gao, J. Dong, and X. Zhang, "On-chip programmable pulse processor employing cascaded MZI-MRR structure," Front. Optoelectron. **12**, 148–156 (2019).
40. Z. Wang, I. Glesk, and L. R. Chen, "An integrated nonlinear optical loop mirror in silicon photonics for all-optical signal processing," APL Photon. **3**, 026102 (2018).
41. Z. Ruan, L. Shen, S. Zheng, and J. Wang, "Subwavelength grating slot (SWGS) waveguide on silicon platform," Opt. Express **25**, 18250–18264 (2017).
42. J. Wang, R. Ashrafi, and R. Adams, "Subwavelength grating enabled on-chip ultra-compact optical true time delay line," Sci. Rep. **6**, 30235 (2016).
43. P. J. Bock, P. Cheben, J. H. Schmid, J. Lapointe, A. Delâge, S. Janz, G. C. Aers, D.-X. Xu, A. Densmore, and T. J. Hall, "Subwavelength grating periodic structures in silicon-on-insulator: a new type of microphotonic waveguide," Opt. Express **18**, 20251–20262 (2010).
44. L. Song, H. Li, and D. Dai, "Mach–Zehnder silicon-photonic switch with low random phase errors," Opt. Lett. **46**, 78–81 (2021).
45. https://www.appliednt.com.
46. S. Chen, Y. Shi, S. He, and D. Dai, "Low-loss and broadband 2×2 silicon thermo-optic Mach-Zehnder switch with bent directional couplers," Opt. Lett. **41**, 836–839 (2016).
47. E. Dulkeith, Y. A. Vlasov, X. Chen, N. C. Panoiu, and R. M. Osgood, "Self-phase-modulation in submicron silicon-on-insulator photonic wires," Opt. Express **14**, 5524–5534 (2006).

91.181.237.252 {ts '2023-06-23 05:13:54'}